remote sensing

MDPI

Article

Oceanic Precipitation Nowcasting Using a UNet-Based Residual and Attention Network and Real-Time Himawari-8 Images

Xianpu Ji [1,3], Xiaojiang Song [2], Anboyu Guo [2], Kai Liu [2], Haijin Cao [1,3] and Tao Feng [1,3,*]

[1] Key Laboratory of Marine Hazards Forecasting, Ministry of Natural Resources, Hohai University, Nanjing 210023, China; xianpuji@hhu.edu.cn (X.J.); h.cao@hhu.edu.cn (H.C.)
[2] Key Laboratory of Marine Hazards Forecasting, National Marine Environmental Forecasting Center, Beijing 100081, China; xjsong@nmefc.cn (X.S.); guoanboyu@nmefc.cn (A.G.); liukai@nmefc.cn (K.L.)
[3] College of Oceanography, Hohai University, Nanjing 210023, China
* Correspondence: fengtao@hhu.edu.cn

Abstract: Qualitative precipitation forecasting plays a vital role in marine operational services. However, predicting heavy precipitation over the open ocean presents a significant challenge due to the limited availability of ground-based radar observations far from coastal regions. Recent advancements in deep learning models offer potential for oceanic precipitation nowcasting using satellite images. This study implemented an enhanced UNet model with an attention mechanism and a residual architecture (RA-UNet) to predict the precipitation rate within a 90 min time frame. A comparative analysis with the standard UNet and UNet with an attention algorithm revealed that the RA-UNet method exhibited superior accuracy metrics, such as the critical ratio index and probability of detection, with fewer false alarms. Two typical cases demonstrated that RA-UNet had a better ability to forecast monsoon precipitation as well as intense precipitation in a tropical cyclone. These findings indicate the greater potential of the RA-UNet approach for nowcasting heavy precipitation over the ocean using satellite imagery.

Keywords: oceanic precipitation nowcasting; deep learning; UNet; attention mechanism; residual network; Himarawi-8 images

Citation: Ji, X.; Song, X.; Guo, A.; Liu, K.; Cao, H.; Feng, T. Oceanic Precipitation Nowcasting Using a UNet-Based Residual and Attention Network and Real-Time Himawari-8 Images. *Remote Sens.* **2024**, *16*, 2871. https://doi.org/10.3390/rs16162871

Academic Editor: Gyuwon Lee

Received: 18 June 2024
Revised: 18 July 2024
Accepted: 4 August 2024
Published: 6 August 2024

1. Introduction

Severe precipitation and associated convective activities pose significant challenges for oceanic safety, leading to hazards such as tropical storms and large ocean waves, which increase navigational risks, resulting in substantial economic losses and casualties [1]. Accurate precipitation forecasts play a vital role in mitigating human and economic losses, offering various social and economic benefits [2–4]. However, predicting heavy precipitation over the open ocean is a significant challenge due to the absence of real-time ground-based observations far from coastal areas. The rapid development, short life cycles, and highly nonlinear dynamics of convective precipitation make precise forecasting difficult [5,6].

The most commonly used approach for precipitation forecasting is numerical weather prediction (NWP) based on numerical models. These models are grounded in the fundamental kinematic and state equations of the atmosphere, thus providing reliable day-to-day weather forecasts. However, NWP encounters challenges referred to as the spin-up problem in nowcasting, affecting forecast accuracy within a three-hour window [6–8]. Consequently, forecasting based on radar observations has emerged as an alternative for precipitation nowcasting. Radar echo reflectivity, along with additional data from sounding, mesonet, and profiler observations [9–11], is often used in radar-echo-based extrapolation for weather nowcasting because of its high temporal and spatial resolution. These techniques involve the identification of convective storms by tracking and extrapolating their movement using techniques such as cross-correlation and optical flow algorithms [12–15]. Subsequently, precipitation rates are estimated based on the empirical correlation between the radar reflectivity factor and precipitation rates, which is known as the Z-R relationship [16,17]. Despite their effectiveness in storm predictions within 30 min, forecast accuracy diminishes with longer lead times [18,19]. Moreover, the high costs of installation and maintenance, alongside the limited radar network coverage, pose obstacles to the widespread application of radar-based precipitation forecasting methods [20–22].

Advancements in satellite-based observations, such as visible/infrared (VIS/IR) images and active/passive microwave data, offer essential atmospheric information for nowcasting over the open ocean. These instruments address existing limitations by providing near-global precipitation datasets and near-real-time imagery. IR-based products enable real-time monitoring and estimation of precipitation with enhanced temporal and spatial resolutions over the open ocean. The VIS/IR methodology relies on identifying convective activity through cold and bright clouds, with colder cloud tops indicating significant vertical development and heavier precipitation. The correlation between IR-derived cloud-top temperatures and surface precipitation intensity allows for the estimation of precipitation from IR data [21,23–27]. Unlike meteorological radar, which directly detects raindrops, satellite VIS/IR images measure the reflectivity or thermal radiation of clouds. Consequently, the latter is less related to the qualitative measurement and forecasting of precipitation; thus, nowcasting oceanic precipitation remains a challenge.

In recent years, deep learning neural network (DNN [28]) techniques have made substantial progress in geophysical research, particularly in the parameterization of model physics [29,30], ENSO prediction [31–33], and precipitation forecasting [34,35]. These advancements have resulted in the possibility of realizing and improving the accuracy of real-time oceanic precipitation nowcasting. Originally, most of these deep learning models were widely used to solve computer vision problems, and they were subsequently gradually proposed to boost the performance of geophysical nowcasting tasks, such as convolutional neural networks [35], recurrent neural networks [36], and Transformers [37,38]. Briefly, an observed precipitation field sequence is treated as a frame of a video used as the input/output of a DNN, which is trained as a forecasting model. These approaches directly predict precipitation at each grid location and have shown promise in predicting low-intensity rainfall using metrics such as the critical success index (CSI), aiming to better model traditionally complex nonlinear precipitation phenomena [39–42], including convective initiation and heavy precipitation [35]. Recently, with the booming use of real radar frames to generate radar frames, generative modeling has attracted much attention, and various models have emerged [43], such as generative adversarial network-based models, e.g., DGMR [8] and GA-SmaAt-GNet [44], as well as diffusion-based models, e.g., Prediff [45] and SRNDiff [46]. Furthermore, with the popularity of the new neural network architecture ViT [47], some works (e.g., FourCastNet [48], Rainformer [49], and Earthformer [50]) have also attempted to apply various Transformer variants [51] to the field of precipitation nowcasting. However, the design of these large Transformer-based models relies on massive samples to learn the underlying laws, which consumes huge computational resources beyond the reach of ordinary researchers [6].

In the field of precipitation nowcasting, a significant milestone was reached by Shi et al. (2015) [39] when they first introduced a neural network model for spatiotemporal forecasting known as convolutional long short-term memory (ConvLSTM) to predict precipitation 90 min ahead using radar-based imagery. The model improved the correlation coefficient by 7% and the detection probability by 5% compared with the conventional optical flow method [52]. This pioneering work has since sparked numerous subsequent studies [6,36,53–59]. From the perspective of models, ConvLSTM-based architectures are capable of modeling the dynamics of the environment, but they often suffer from mode-averaging and limited long-term dependencies between sequence elements [60]. In addition, the structure of ConvLSTM is considered relatively fixed due to its foundation on LSTM integrated with convolutional operations, which makes it difficult to efficiently capture and process complex spatial details and pixel-level prediction tasks. The UNet architecture is based on multilayer convolutional neural networks and offers greater flexibility in processing different types of data by modifying the structure of the encoder and decoder; it is similar to a convolutional neural network but is better suited for pixel prediction (predicting the rates of precipitation at each grid point) [5,61–63] than ConvLSTM-based models. UNet is increasingly used in spatiotemporal forecasting studies, such as in those of nowcasting of lightning [63,64] and floods [65].

Although many forecasting models for precipitation have been developed, they are usually based on ground-based radar observations. Only a few studies have designed deep learning models for precipitation nowcasting using satellite data [42,66,67], especially for oceanic precipitation nowcasting. More recently, the Integrated Multi-Satellite Retrievals for Global Precipitation Measurement (IMERG [68]) satellite data and Global Forecast System (GFS) forecasts ([69]) were used [66] to train neural networks by fusing a UNet and a convolutional long short-term memory (LSTM) neural network for the nowcasting of precipitation almost globally every 30 min with a 4 h lead time. The results showed the potential of IMERG for oceanic precipitation nowcasting at high spatial and temporal resolutions. Despite these advances, there is still a lack of research on oceanic precipitation nowcasting. Therefore, in this study, high-resolution satellite data were utilized to study near-real-time oceanic precipitation nowcasting.

Furthermore, recent studies demonstrated that attention mechanisms [70] and residual architectures [71] can significantly enhance prediction performance. Both of these methods are enhanced by a skip connection [72], which allows for a better comparison with the original UNet. In the attention UNet established by Oktay (2018) [70], attention gates (AGs) are added to the skip connections to maintain a high prediction accuracy without the need for an external organ localization model [72]. In addition, residual blocks address the problem of vanishing gradients, which often occur when stacking multiple layers in a deep neural network, as well as the degradation problem, which leads first to saturation and then to the degradation of accuracy as more and more layers are added to the network, thus enabling deeper network architectures [71].

Consequently, this study employs UNet as the backbone model for oceanic precipitation nowcasting and explores the capabilities of UNet, the attention UNet (Att-UNet), and the residual UNet with attention (RA-UNet). The paper extends previous efforts to the open ocean where high-resolution observations are lacking. The satellite observations with high temporal and spatial resolution (0.1° $\times$ 0.1°, 30 min) over the ocean are utilized to construct an oceanic precipitation nowcasting model. Then, the UNet and two variant architectures (Att-UNet and RA-UNet) are examined, which promise improved nowcasting of oceanic precipitation extremes. The rest of this paper is organized as follows: Section 2 describes the data, evaluation methods, and experimental design; Section 3 describes the preprocessing approach and UNet architectures with an attention mechanism and a residual structure; Section 4 evaluates and interprets the results; and Section 5 concludes and discusses the findings.

2. Data and Methodology

2.1. Data

This study aims to evaluate several UNet-based deep learning models in their prediction of oceanic precipitation in the next 1.5 h in a limited area over the tropical western North Pacific Ocean, covering 119.2°–131.9°E, 12.8°–25.59°N. This area features a hot and humid climate, with frequent monsoonal convection activity and tropical cyclones. Himawari-8 is of the new generation of geostationary satellites, providing near-real-time observations of eastern Asia, and its bright temperature data have been widely used for the spatial coverage of convection [61], as well as for the prediction of extreme precipitation events [73]. Thus, Himawari-8 serves as a superior proxy for near-real-time prediction with an extensive spatial range and was used in this study as the predictor in the deep learning model, as illustrated in Figure 1a–g. Launched by the Japan Meteorological Agency (JMA) in October 2014 [74], this geostationary meteorological satellite (GMS) provides sixteen observation bands, including three visible bands, three near-infrared bands, and ten infrared bands (Table 1). The observation bands of the satellite facilitate the understanding of vegetation, aerosol, sea-surface temperature, cloud, and moisture conditions. Additionally, the spatial resolutions of the observations are 0.5–1.0 km for visible bands and 1.0–2.0 km for near-infrared and infrared bands. Seven of the infrared bands associated with precipitation, each with a spatial resolution of 2 km every 10 min, were employed, as suggested by Lagerquist et al. (2021) [61] (Table 1). Furthermore, all seven brightness temperature bands (8, 9, 10, 11, 13, 14, 16) are in the infrared part of the spectrum and have traditionally been used to forecast convection due to their greater interpretability in comparison with infrared radiation. In this study, the brightness temperature was utilized as a predictor for the model. Finally, the spatial resolution of the model was $0.1^\circ \times 0.1^\circ$, covering a total of 128×128 grid points every 30 min.

The ground-truth data for the model input were sourced from the Integrated Multi-Satellite Retrievals (IMERG) for the Global Precipitation Measurement (GPM) dataset [68] (Figure 1h). The IMERG product provides gridded high-resolution estimates of precipitation rates with a spatial resolution of 0.1°every 30 min, and it is calibrated based on the deviation of the monthly observation data from ground rainfall stations. These data have been widely used in precipitation forecasting to fill in gaps where radar coverage is limited [22,66]. IMERG products offer the significant advantages of providing near-global (from 60°S to 60°N) precipitation estimates from March 2014 onward, integrating data from passive microwave and infrared satellites within the GPM constellation. The precipitation rate variables are provided in near real time —marked as IMERG Early and Late—and as post-real-time research data, i.e., IMERG Final, after incorporating a monthly rain gauge analysis. For this study, even the Early data had a time delay of 4 h, which made it difficult to use them for real-time forecasting, but the precipitation products were sufficiently reliable without taking the errors in the data themselves into account, so the L3 final precipitation product from IMERG version 6 was used here as the true value for validation purposes. Ultimately, data from 1 January 2017 to 31 December 2018 were used, with the 2017 data being divided into a training set and a validation set for model training, while the 2018 data were used as a test set for model evaluation.

Table 1. Characteristics of the spectral bands of Himawari-8.

Band No.	Central Wavelength (μm)	Spatial Resolution (km)	Physical Properties	Usage
1 (visible)	0.47	1	Vegetation, aerosol	No
2 (visible)	0.51	1	Vegetation, aerosol	No
3 (visible)	0.64	0.5	Vegetation, low cloud, fog	No
4 (Near-infrared)	0.86	1	Vegetation, aerosol	No
5 (Near-infrared)	1.6	2	Cloud phase	No
6 (Near-infrared)	2.3	2	Particle size	No
7 (Infrared)	3.9	2	Low cloud, fog, forest fire	No
8 (Infrared)	6.25	2	Mid- and upper-level moisture	Yes
9 (Infrared)	6.95	2	Mid-level moisture	Yes
10 (Infrared)	7.35	2	Mid- and lower-level moisture	Yes
11 (Infrared)	8.6	2	Cloud phase	Yes
12 (Infrared)	9.6	2	Ozone content	No
13 (Infrared)	10.45	2	Cloud imagery, information of cloud top	Yes
14 (Infrared)	11.2	2	Cloud imagery, sea-surface temperature	Yes
15 (Infrared)	12.4	2	Cloud imagery, sea-surface temperature	No
16 (Infrared)	13.3	2	Cloud-top height	Yes

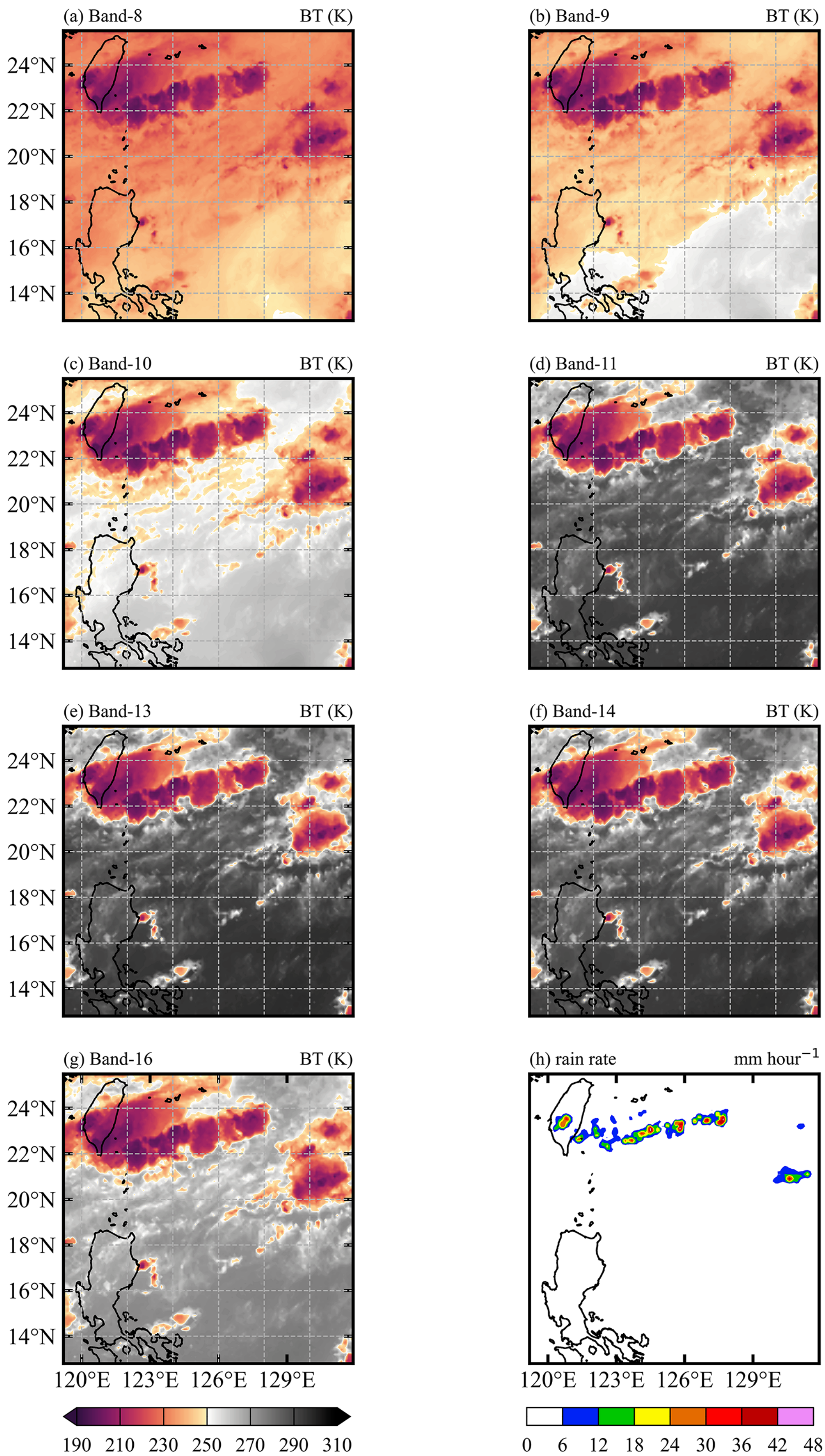

Figure 1. An example of the input data valid at 1800 UTC on 3 June 2017. (**a**–**g**) Brightness temperature (K) in each spectral band from the Himawari-8 satellite images; (**h**) precipitation rate from the GPM IMERG products (mm h^{-1}).

2.2. Evaluation Methods

Three metrics were used for model verification: the probability of detection (POD), false alarm ratio (FAR), and critical success index (CSI; Table 2 [75]). The POD was used to assess the model's accuracy in predicting events according to the ratio of correct predictions to the total number of actual events. The FAR was used to gauge the rate of false alarms in model predictions according to the ratio of the number of false alarms (incorrectly predicted events) to the total number of predicted events. The CSI, also known as the threat score (TS), provides a comprehensive evaluation of a model's predictive skill by combining hits, misses, and false alarms. The CSI is the ratio of correct predictions to the sum of actual events and false alarms.

The metrics of the CSI, POD, and FAR all range from 0 to 1, with a perfect score of 1. Higher values indicate better performance for both the POD and CSI, while a lower FAR value represents better performance in reducing false alarms. It should be recalled that in the CSI metric, the elements of a confusion matrix are determined for a binary representation of the precipitation fields with the rates above a prespecified threshold in mm h^{-1}. To evaluate the performance of the regression network using the classification scores, three thresholds were set: 0.1 mm h^{-1} (also treated as a rainfall forecast), 1 mm h^{-1}, and 5 mm h^{-1}.

Table 2. The true-positive (TP), true-negative (TN), false-positive (FP), and false-negative (FN) rates characterize the confusion matrix. TP refers to the number of grid pixels where both the observed and predicted rain rates are greater than the threshold; FP refers to the number of grid pixels where the observed rain rate is lower than the threshold, while the predicted rain rate is greater than the threshold; FN refers to the number of grid pixels where the observed rain rate is greater than the set threshold, while the predicted rain rates are lower than the threshold. These three metrics serve as benchmarks for assessing prediction accuracy.

Score	Definition	Range	Optimal Value
Probability of detection (POD)	$TP/(TP+FN)$	[0, 1]	1
False-alarm ratio (FAR)	$FP/(FP+TP)$	[0, 1]	0
Critical success index (CSI)	$TP/(TP+FN+FP)$	[0, 1]	1

2.3. Experimental Design

The precipitation nowcasting problem is defined as predicting the precipitation rate for the upcoming 1.5 h in 30 min intervals by utilizing brightness temperature data from 3 h prior, as shown in Equation (1).

$$\hat{P}_{t+30\mathrm{min}}, \ldots \hat{P}_{t+90\mathrm{min}} = \mathcal{M}\left(\hat{B}_{t-150\mathrm{min}}, \ldots \hat{B}_{t0}\right), \tag{1}$$

where $\mathcal{M}$ represents the deep learning model for nowcasting, and each instance contains data of 9 time steps in total. The observations from Himawari-8 at various time steps are stacked together to create the channel dimension. Finally, each input sample for the model consists of 6 time steps (past Himawari-8 brightness temperatures) spanning 7 bands with a size of 128 × 128. The model output samples are 3 time steps (future precipitation rates) with a size of 1 × 128 × 128. For each initial time t_0, precipitation nowcasting is available only if the following hold:

1. The Himawari-8 satellite data used as predictors are accessible at all necessary time lags (t_0, $t_{-30\mathrm{min}}$, $t_{-60\mathrm{min}}$, $t_{-90\mathrm{min}}$, $t_{-120\mathrm{min}}$, and $t_{-150\mathrm{min}}$);
2. The GPM satellite data, which act as labels, are obtainable at the required future times ($t_{+30\mathrm{min}}$, $t_{+60\mathrm{min}}$, and $t_{+90\mathrm{min}}$).

Three experiments, namely, experiments with UNet, Att-UNet, and RA-UNet, were conducted by utilizing the UNet architecture to evaluate the influence of incorporating attention and recurrent residual mechanisms into the model. Att-UNet integrated attention gates to refine the features transmitted via the skip connections within the UNet framework, while RA-UNet incorporated a residual structure into Att-UNet. The specifics of these models are elaborated on in the subsequent section.

The loss function used to optimize the UNet parameters during training was the mean absolute error (MAE), also referred to as the L1 loss, which is utilized in regression tasks to calculate the average absolute disparities between predicted values from a model and the actual target values. For instance, the MAE is defined as

$$MAE = \frac{\sum_{i=1}^{n} \left| \left(y_{\text{pred}} \right)_i - \left(y_{\text{target}} \right)_i \right|}{n} \quad (2)$$

3. Preprocessing and Model Architecture

3.1. Preprocessing Processes

The data preprocessing processes are depicted in Figure 2. As the GPM precipitation data had a maximum resolution of 0.1° every 30 min, the Himawari-8 satellite data were interpolated from 2 km × 2 km to 0.1°× 0.1° for consistency and computational efficiency (Figure 2).

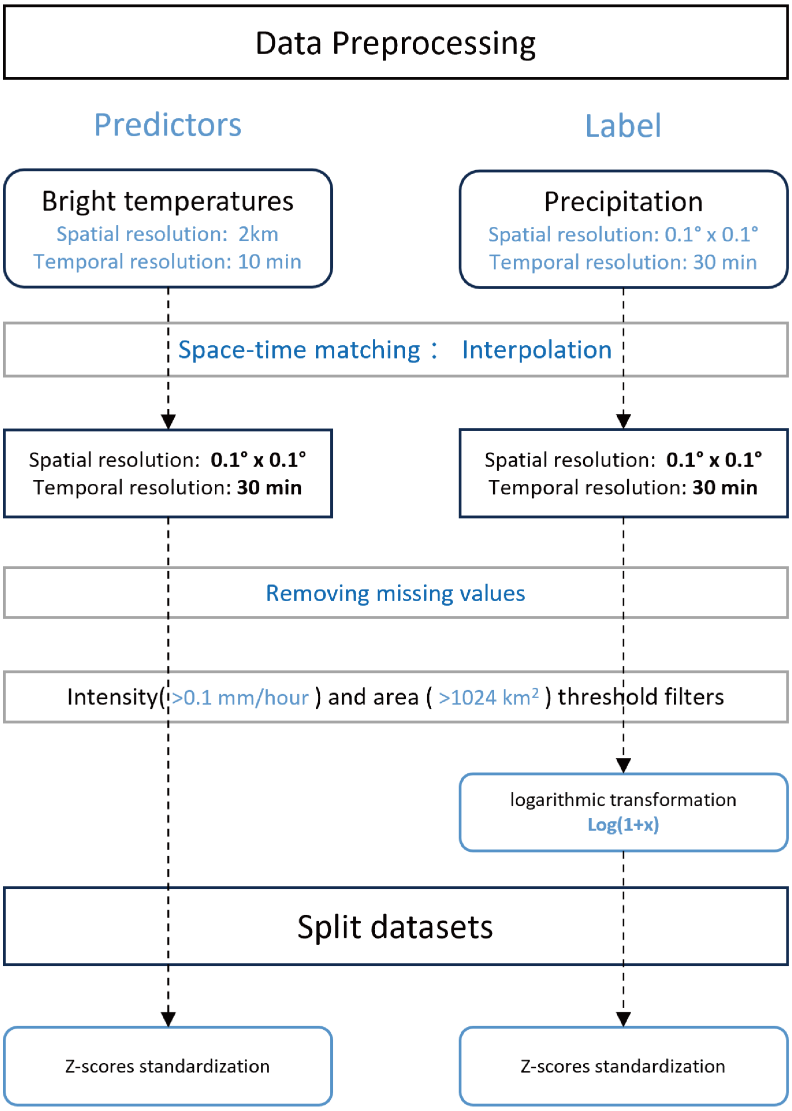

Figure 2. Flowchart of data preprocessing for the Himawari-8 and GPM datasets.

Following the interpolation process, adjustments were made to both the brightness temperature and precipitation fields to facilitate the generation of 30-minute-interval forecasts. Moreover, instances of extraneous noise within the interpolated brightness temperature dataset were identified as missing values and subsequently excluded from both the brightness temperature and precipitation variables at specific intervals. It was observed that a considerable fraction of precipitation measurements fell within the range from 0.0 to 1.0 mm h^{-1}, indicating notable right skewness. This distribution skewness is commonly associated with the relatively high frequency of clear days [76]. Generally, the alleviation of right skewness can greatly enhance the clarity of data patterns. Hence, a logarithmic transformation that specifically used $log(x+1)$, in conjunction with a filtering technique, was employed to condense the skewed data [77]. As shown in Figure 3, the skewness was greatly reduced after the transformation.

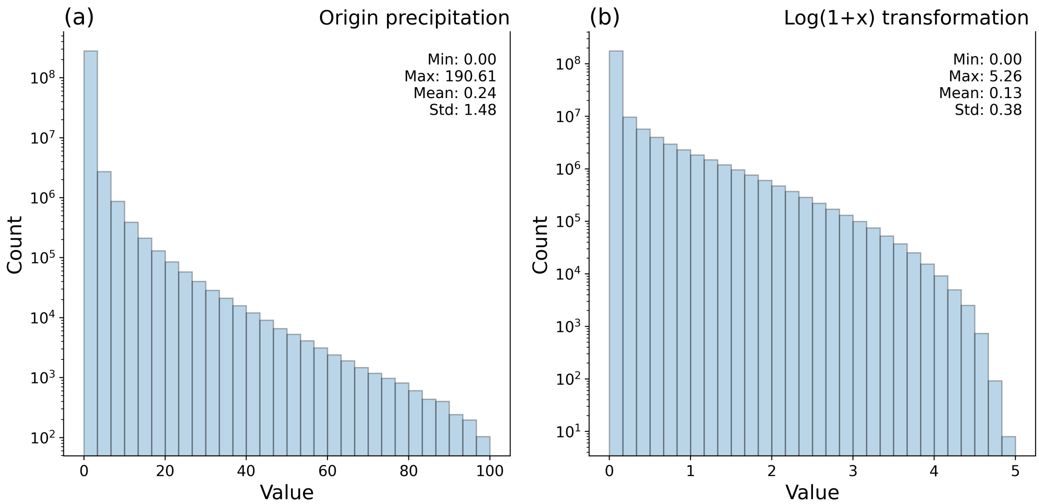

Figure 3. Probability density function of precipitation samples from the GPM data (unit: mm h^{-1}) before (**a**) and after (**b**) performing the $log(1+x)$ transformation.

The preprocessing process involved setting up both an intensity threshold and an area threshold. At each time step of the GPM data, the area within the rain rate data that exceeded the intensity threshold was computed and recorded as the area evaluation [5]. If the peak of area evaluations was determined to be lower than the area threshold, the data sample was classified as "non-rainy" and consequently omitted from the datasets. Practically, the intensity and area thresholds were set to 0.1 mm h^{-1} and 1024 km^2, respectively. This area size was large enough to capture precipitation phenomena relevant to our study and efficiently excluded non-rainy samples without compromising the integrity of the data distribution.

Following the exclusion of non-rainy days, the dataset contained 12,740 samples for analysis. In the final preparation step before model input, both the brightness temperature and rain rate data were normalized using z-score standardization as follows:

$$var_{std} = \frac{var - mean(var)}{stddev(var)} \tag{3}$$

In addition, for training and validation purposes, the data from the year 2017 were utilized with a split ratio of 7:3. The testing period covered the full year of 2018.

3.2. Model Architecture

In this study, a sophisticated variant of the UNet architecture known as Res-UNet with attention (RA-UNet) [78] was employed to enhance the accuracy of rainfall rate predictions, as depicted in Figure 4. The model is based on the UNet architecture proposed by Ronneberger et al. (2015) [79]. The whole network structure is shaped like the letter "U", so it is named UNet. The U-shaped model consists of four main components, which are shown in Figure 4: convolutional layers, pooling (for downsampling), upsampling layers, and skip connections. The left-hand side is the downsampling side, that is, the encoding process, and the right-hand side is the upsampling side, that is, the decoding process. The convolutional layers are responsible for identifying spatial features, and their coordinated operation with other components allows distinct convolutional layers to capture features across different resolutions. This capability is crucial for predicting weather phenomena due to their inherent multiscale complexities [61]. The initial layer takes raw predictors as inputs, and subsequent layers receive transformed versions of these raw predictors, which are known as feature maps. Through the convolution process, which involves both spatial and multivariate transformations, these feature maps effectively encode spatial patterns that encompass all predictor variables. Additionally, within the framework of a convolutional neural network or UNet, a nonlinear activation function is systematically applied after each convolutional layer.

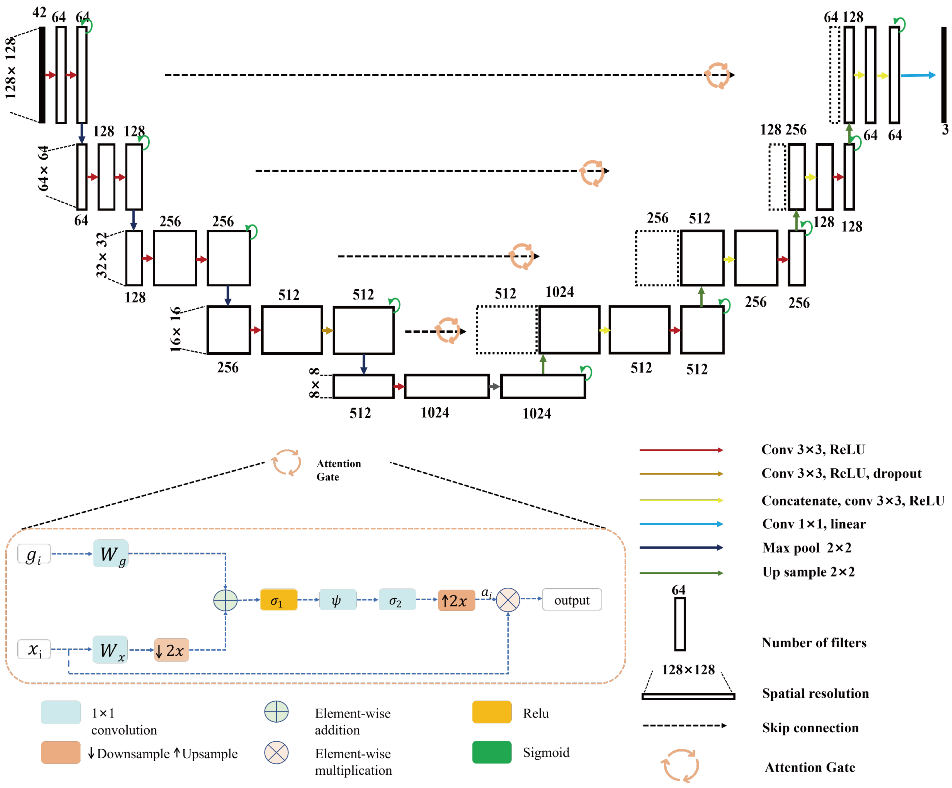

Figure 4. A diagram of RA-UNet.

In the UNet architecture, each pooling layer reduces the spatial resolution of the feature maps using a 2 × 2 maximum filter. To compensate for the loss of spatial information, the number of feature maps typically increases to offset the loss of spatial information. On the other hand, each upsampling layer increases the spatial resolution of the feature maps using interpolation followed by convolution. The convolution step is crucial because interpolation alone cannot effectively reconstruct high-resolution information from low-resolution counterparts. In this process, the number of channels typically decreases as the spatial resolution increases, ultimately reaching the number of output channels. Additionally, skip connections play a crucial role in preserving high-resolution information from the downsampling side and transferring it to the upsampling side. Without skip connections, the UNet architecture would suffer from cumulative loss of spatial information due to successive downsampling and upsampling operations. This loss is referred to as a “lossy operation” [79] and reduces the network’s ability to reconstruct high-resolution features in the output accurately.

Building on UNet, attention UNet (Att-UNet) [70] was developed by integrating an additive attention gate, enhancing model sensitivity and prediction accuracy with minimal computational overhead. Attention gates filter the features transmitted through the skip connections. Primarily, input features are adjusted with attention coefficients calculated in the attention gate. Spatial regions are selected by examining both activations and contextual information provided by the gating signal, which is obtained from a coarser scaler. Attention coefficients are interpolated using trilinear interpolation. Similar to the UNet architecture, Att-UNet treats channels and lag times equivalently.

Lastly, Res-UNet with attention (RA-UNet) is derived by utilizing an attention gate and residual convolutional unit based on the traditional UNet. When compared with regular forward convolutional units, a residual unit (Figure 5) is beneficial when training deep architectures and significantly impacts model performance [71]. In RA-UNet, channels and lag times are also treated equivalently.

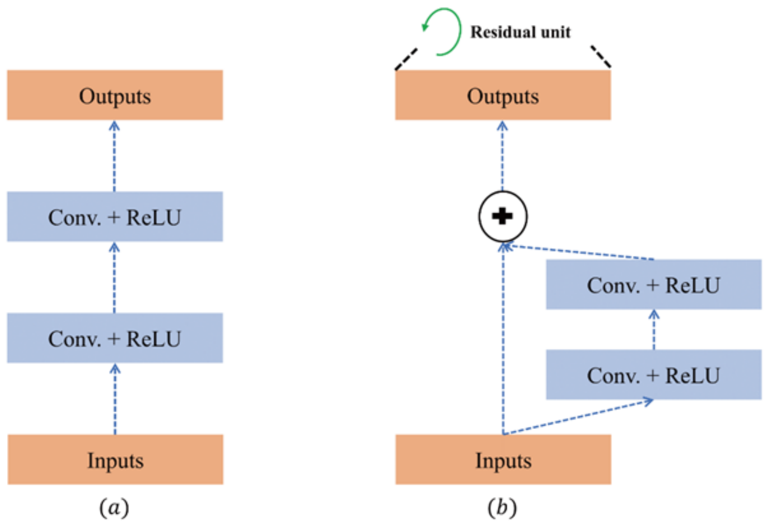

Figure 5. Different variants of convolutional and recurrent convolutional units: (**a**) forward convolutional units; (**b**) residual convolutional units.

4. Results

4.1. Quantitative Evaluation

The nowcasting accuracy of three distinct models on the testing dataset was rigorously accessed by employing the CSI at thresholds of 0.1, 1.0, and 5.0 mm h^{-1}. As shown in Figure 6, the CSI metrics of all models surpassed the benchmark of 0.27 at the 0.1 mm h^{-1} threshold, suggesting relatively reliable performance in forecasting precipitation events with 30–90 min of lead time. Notably, for moderate and heavy rainfall intensities, a discernible decline in the CSI values was observed, diminishing to approximately 0.18–0.26 and less than 0.10, respectively. Among these models, RA-UNet demonstrated superior efficacy, which was particularly conspicuous in events exceeding 5.0 mm h^{-1}, where its CSI was observed to be double that of its counterparts, underscoring its enhanced prediction skill for enhanced rainfall events.

The POD metric revealed uniformity across the models at a threshold exceeding 0.1 mm h^{-1}, with each approximating a POD score of 0.35–0.50. However, a pronounced decrement was noted as the precipitation rate intensified. The RA-UNet model exhibited slightly superior performance at the 0.1 mm h^{-1} threshold in comparison with the other models; moreover, it maintained a POD score of 0.06–0.12 in heavy rainfall conditions, illustrating its robustness in forecasting severe precipitation events, in distinct contrast to UNet and Att-UNet, which exhibited negligible predictive accuracy under similar conditions.

An evaluation of the FAR further distinguished the models' performance across varying precipitation thresholds. At the 0.1 mm h^{-1} threshold, the highest FAR values for RA-UNet were comparable to the other two models. However, RA-UNet achieved the lowest FAR at increased thresholds of 5 mm h^{-1}. This trend suggested that the RA-UNet model was predisposed toward predicting more intense rainfall, thereby enhancing both the POD and CSI.

Figure 6 also shows an evaluation of the changes in the CSI, POD, and FAR metrics across various forecast lengths for different models. It was observed that with an increase in the forecast length, the forecast performance of these models tended to decline. This decline was characterized by an increase in the FAR alongside decreases in the POD and CSI. Specifically, for the CSI metric, the UNet and Att-UNet models exhibited a downward trend for the 0.1 mm h^{-1} threshold as the forecast period extended from 30 to 90 min. Conversely, the RA-UNet model demonstrated more stability in its forecasts, regardless of whether they pertained to clear or rainy conditions. In scenarios of moderate to heavy rainfall, it was noted that the CSI scores for all three models showed a marked decrease. However, for heavy rainfall events and a forecast lead time of 30 min, the RA-UNet model achieved a CSI score of 0.1, outperforming the other models at the 30 min forecast length. This superior performance of the RA-UNet model was also reflected in the POD and FAR, indicating a longer period of relatively reliable forecast availability for this model.

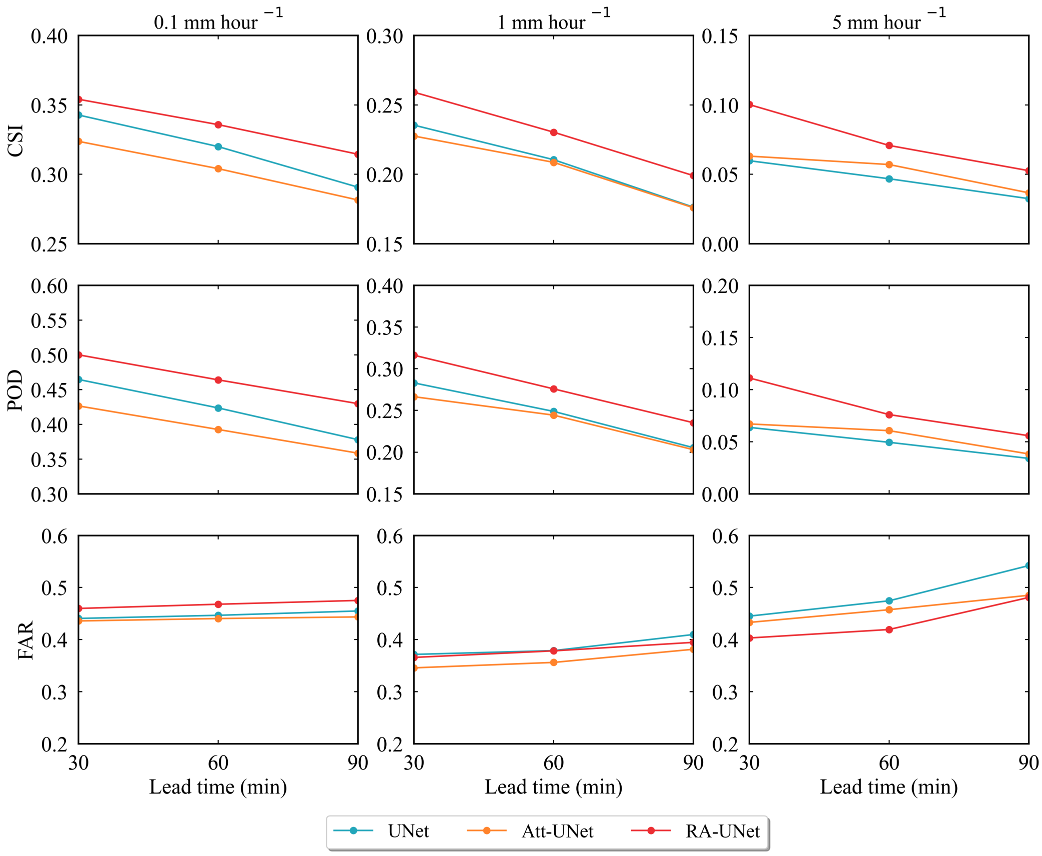

Figure 6. The critical success index, probability of detection, and false alarm ratio for three different intensity thresholds (0.1, 1, and 5 mm h^{-1}). The metrics are shown as a function of the lead time. The blue, orange, and red lines, respectively, represent the forecast performance of the UNet model, Att-UNet model, and RA-UNet model with the lead time.

Considering the strong seasonal features of precipitation, it was necessary to evaluate the performance of the model in simulating precipitation for each month. The performance of the three models for each month of 2018 is shown in Figure 7. Overall, it can be observed that the performance of the three models for oceanic precipitation nowcasting showed clear seasonal characteristics. For 0.1 mm h^{-1}, the CSI was highest during the boreal summer season (June/July/August), which corresponded to a high POD and a low FAR, which may be attributed to the fact that heavy precipitation is more likely to occur in the summer months. In contrast, the CSI was lowest in the spring season (March/April/May), which corresponded to a low POD and a high FAR, which may have been related to the fact that spring is characterized by lower precipitation and a more complex nonlinear process [80]. In addition, RA-UNet had better performance than that of the other two models, especially in the spring season. Meanwhile, RA-UNet tended to perform better in the summer season compared with UNet and Att-UNet for moderate and heavy precipitation, which reflected the potential of the model for summertime oceanic precipitation prediction. For heavy precipitation at 5 mm h^{-1}, the FAR of the three models showed missing values in March, as no positive cases were detected in this month.

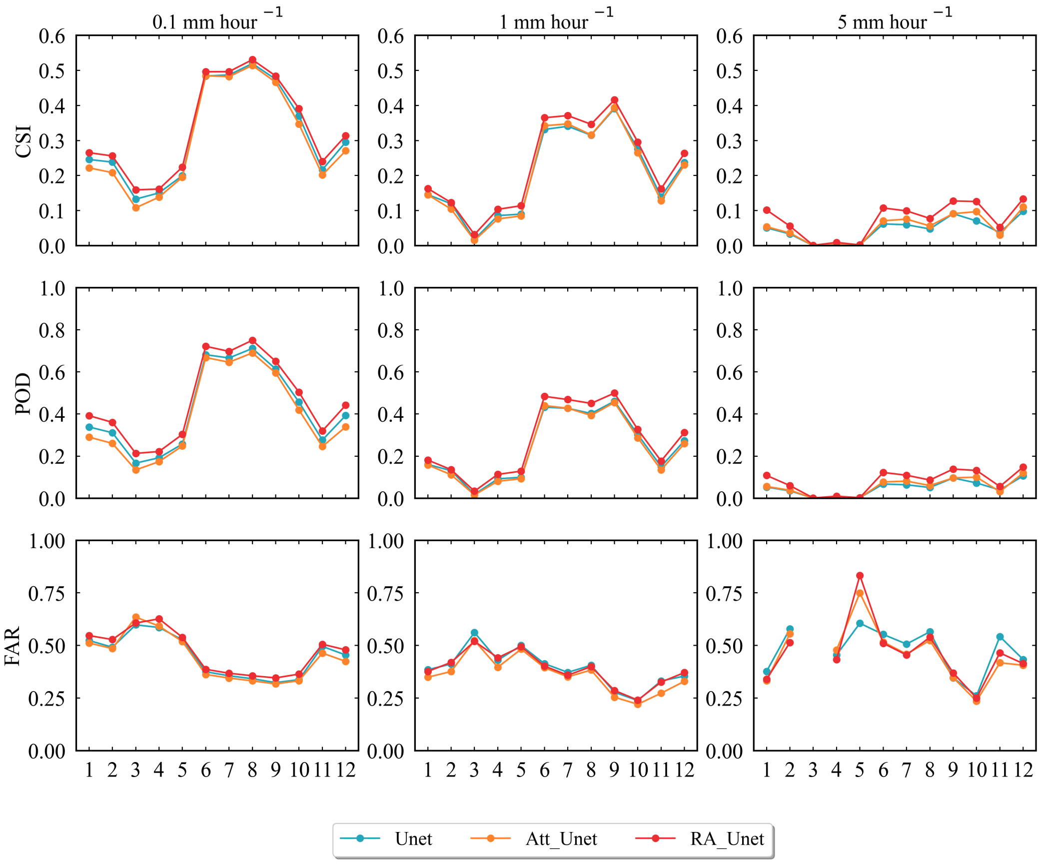

Figure 7. The critical success index (CSI), probability of detection (POD), and false alarm ratio (FAR) for three different intensity thresholds (0.1, 1, and 5 mm h^{-1}) averaged over 30–90 min forecasts for each month of 2018. The metrics are shown as a function of the month. The blue, orange, and red lines, respectively, represent the forecast performance of the UNet model, Att-UNet model, and RA-UNet model in each month.

4.2. Examples

Two typical examples are provided: one of summer monsoon rainfall induced by a monsoon trough and another of rainfall caused by a typhoon. An individual case of monsoon precipitation demonstrated the efficacy of the three distinct models, as depicted in Figure 8. This figure illustrates the inputs (brightness temperatures labeled in Figure 8a–c), the evaluation truth (rain rates labeled in Figure 8d–f), and the outputs from the three models—UNet, Att-UNet, and RA-UNet (represented in Figure 8g–o and depicting the rain rates). For the purpose of brevity, only the visual representations from one band (band 16) are exhibited. The input sequence (Figure 8a–c) highlighted three regions with cooler brightness temperatures (corresponding to areas A, B, and C in Figure 8d–f). Diminished brightness temperatures, on the other hand, usually indicated the development of convective clouds that favor precipitation formation [81], suggesting a heightened likelihood of precipitation in these locales. Subsequently, the evaluation truth (Figure 8d–f) revealed a progressive diminution in the rain cloud densities in areas A, B, and C. This subtle attenuation of precipitation intensity was adeptly captured by all three models, although the detection of heavy precipitation remained an area necessitating enhancement. Among the three, the RA-UNet model outperformed its counterparts in the 1.5 h nowcast for the triad of precipitation clouds across areas A, B, and C, particularly excelling in mapping the evolution of the rain cloud in sector C. This notable performance was likely due to the inclusion of a residual structure within the model. This result coincided with the analysis in Figure 6, which shows that the model with a residual structure exhibited better performance. Conversely, the UNet and Att-UNet models exhibited moderate performance, managing only to approximately delineate the spatial distribution of the rain clouds in areas A and B, with predictions for cloud C being notably less distinct. Additionally, the enhancements brought forth by the implementation of Att-UNet appeared to be marginal in comparison with the base UNet model, which was potentially due to an insufficiency of training samples specific to this forecasting task.

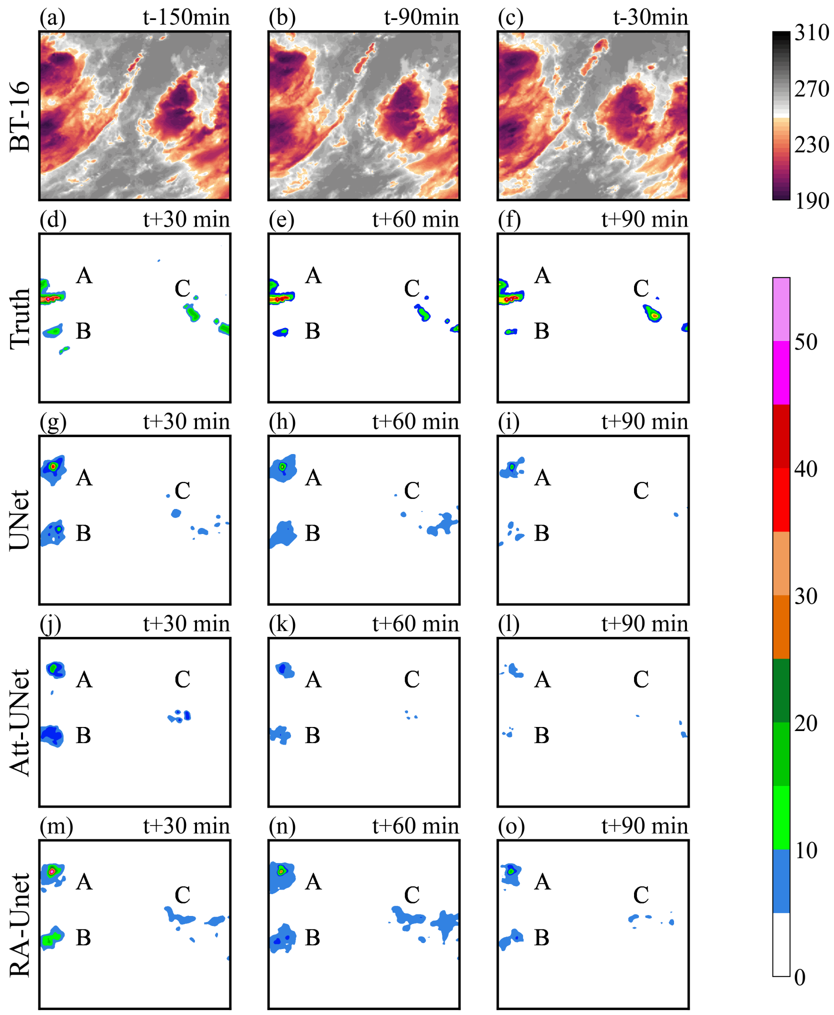

Figure 8. An example of a forecast during a summer monsoon. The brightness temperature (band 16) of inputs (**a**–**c**), the ground truth (**d**–**f**), and nowcasts from the UNet (**g**–**i**), Att-UNet (**j**–**l**), and RA-UNet (**m**–**o**) models corresponding to 30 min (first column), 60 min (second column), and 90 min forecasts.

During the testing period, a tropical cyclone event was observed to evaluate the predictions of three models for heavy precipitation events. Tropical cyclone "Yutu", also known as Super Typhoon Rosita in the Philippines, was a powerful tropical storm with extremely heavy rainfall that caused widespread destruction on the islands of Tinian and Saipan in the Northern Mariana Islands before moving on to impact the Philippines. It formed on 21 October 2018 and dissipated on 3 November. For the forecast time from 11:30 a.m. to 5:00 p.m. on 29 October 2018, the prediction results of the three models are displayed in Figure 9. Similar to Figure 8, clear areas of vortex precipitation were detected when the typhoon had already developed and matured. The prediction results revealed that, overall, all three models were able to capture the evolving prediction of heavy precipitation during typhoons. However, the UNet model showed weaknesses in capturing the intensity of precipitation during the typhoon, while the Att-UNet model showed some improvement. In contrast, the RA-UNet model demonstrated a better ability to capture the precipitation intensity and its evolutionary development, consistent with the previous result that the RA-UNet model was better for predicting extreme precipitation.

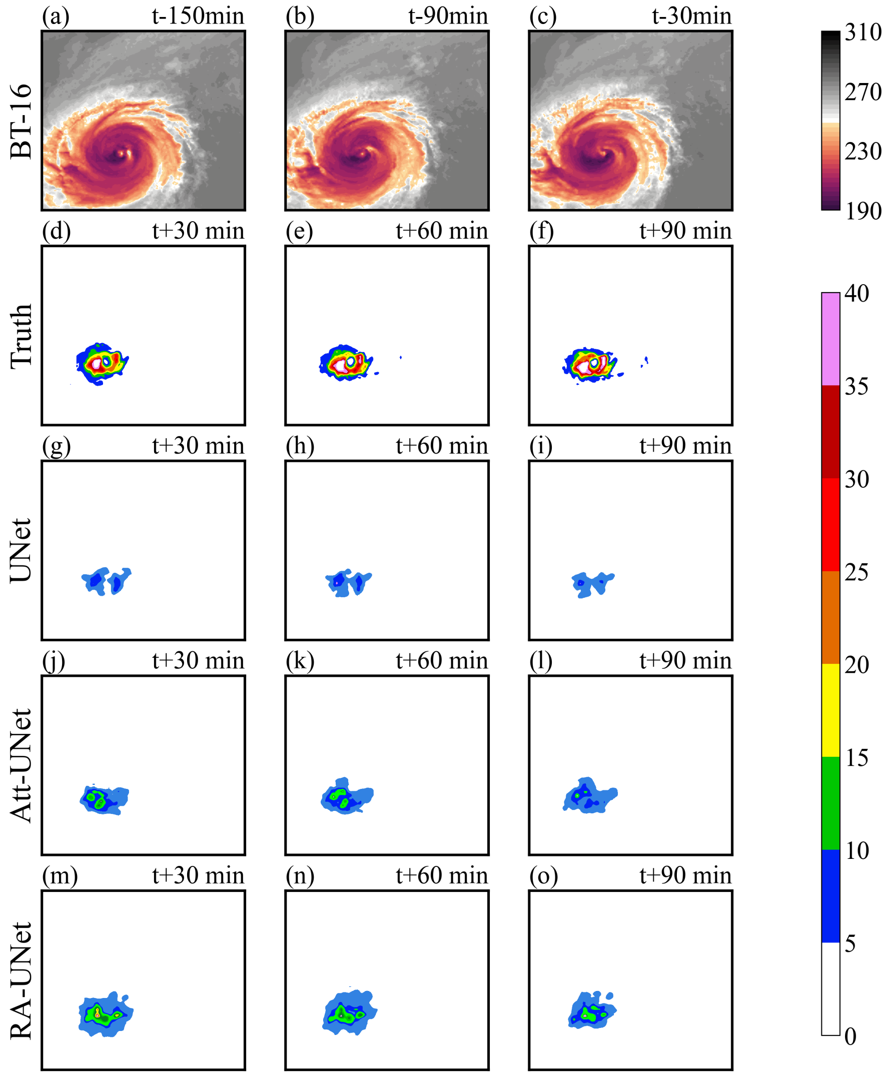

Figure 9. A prediction example that occurred during a typhoon. Brightness temperature (band 16) of inputs ((**a**–**c**), 29 October 2018 at 11:30, 12:30, and 13:30, respectively), ground truth ((**d**–**f**), 29 October 2018 at 14:30, 15:00, and 15:30, respectively), and nowcasts from the UNet (**g**–**i**), Att-UNet (**j**–**l**), and RA-UNet (**m**–**o**) models corresponding to 30 min (first column), 60 min (second column), and 90 min forecasts.

5. Discussion and Conclusions

The present study developed a UNet-based approach to predict the oceanic rainfall rate using Himawari-8 satellite images and GPM precipitation products. The satellite observations underwent preprocessing steps, including spatiotemporal matching, missing value handling, threshold filtering, logarithmic transformation, and z-score standardization, to prepare them to train the prediction models. Then, the models were evaluated using a dataset of nearly one year. The quantitative assessments demonstrated that all three UNet-based models had the ability to provide oceanic precipitation predictions within 30–90 min, with higher accuracy during boreal summer. By incorporating the attention mechanism and residual structure, the RA-UNet model exhibited superior accuracy for oceanic precipitation nowcasting than other models, especially for heavy convective rainfall. This highlights its potential for nowcasting heavy oceanic convective rainfall, such as typhoon rainfall, as indicated by a typical case. The RA-UNet model presents a promising opportunity for deep learning models to advance the nowcasting of oceanic precipitation.

This study demonstrates the applicability of satellite images to oceanic precipitation nowcasting through deep learning methods that are potentially applicable to real-time nowcasting. However, due to limited computational resources, only two years of data were used for training and validation, and the relationship between the input variables and the true values may not have been completely captured. Augmenting the volume of experimental data may enhance the accuracy and reliability of the network model. Additionally, the temporal and seasonal variability of precipitation data need to be examined in future work. Season-specific predictions could be developed, particularly in winter, when there is less convective activity, as well as during the spring, when more complex precipitation processes occur [82]. The problem of imbalance between precipitation data samples in the spring and winter seasons can be solved by increasing the weight of relevant precipitation data during the training process. Furthermore, while bright cloud-top temperatures provide information about cloud properties and the related convection intensity, the absence of three-dimensional dynamic and thermodynamic structures may reduce the reliability of deep neural network models. Future work will consider incorporating other predictors, such as forecasts of numerical weather models that illustrate the three-dimensional atmospheric state, to improve the model's forecasting capability and interpretability [61]. Furthermore, this study could also benefit from recent advancements in deep-learning models such as SmaAt-UNet and EarthFormer. These models may prove valuable in enhancing forecast accuracy and optimizing the operational efficiency of the predictive model. These results will be reported in the near future.

Author Contributions: Conceptualization, T.F. and X.J.; methodology, X.J.; formal analysis, X.J. and T.F.; resources, A.G. and K.L.; writing—original draft preparation, X.J.; writing—review and editing, X.J. and T.F.; visualization, X.J.; project administration, X.S. and H.C. All authors have read and agreed to the published version of the manuscript.

Funding: This study was supported by the National Key R&D Program of China (2023YFC3008003), the National Natural Science Foundation of China (42175063), and Guangxi Key Laboratory of Marine Environmental Change and Disaster in Beibu Gulf (Beibu Gulf University) (2023KF04).

Data Availability Statement: The Himawari-8 satellite data are publicly available at https://www.eorc.jaxa.jp/ptree/index.html (accessed on 3 August 2024), and the GPM data are available at https://doi.org/10.5067/GPM/IMERG/3B-HH/07 (accessed on 3 August 2024).

Acknowledgments: The authors appreciate the editor and two anonymous reviewers for their valuable comments. They also acknowledge Yu Zheng from Nanjing Joint Institute for Atmospheric Sciences and Zikang He from Hohai University for their helpful advice on the modeling and data-handling processes in this work.

Conflicts of Interest: The authors declare no conflicts of interest.

References

1. Seneviratne, S.I.; Zhang, X.; Adnan, M.; Badi, W.; Dereczynski, C.; Luca, A.D.; Ghosh, S.; Iskandar, I.; Kossin, J.; Lewis, S.; et al. *Weather and Climate Extreme Events in a Changing Climate*; Cambridge University Press: Cambridge, UK, 2021.
2. Brown, B.G.; Katz, R.W.; Murphy, A.H. On the economic value of seasonal-precipitation forecasts: The fallowing/planting problem. *Bull. Am. Meteorol. Soc.* **1986**, *67*, 833–841. [CrossRef]

3. Hartman, B.; Cutler, H.; Shields, M.; Turner, D. The economic effects of improved precipitation forecasts in the United States due to better commuting decisions. *Growth Chang.* **2021**, *52*, 2149–2171. [CrossRef]
4. Shrader, J.G.; Bakkensen, L.; Lemoine, D. *Fatal Errors: The Mortality Value of Accurate Weather Forecasts*; Technical report; National Bureau of Economic Research: Cambridge, MA, USA, 2023.
5. Pan, X.; Lu, Y.; Zhao, K.; Huang, H.; Wang, M.; Chen, H. Improving Nowcasting of convective development by incorporating polarimetric radar variables into a deep-learning model. *Geophys. Res. Lett.* **2021**, *48*, e2021GL095302. [CrossRef]
6. Ma, Z.; Zhang, H.; Liu, J. MM-RNN: A multimodal RNN for precipitation nowcasting. *IEEE Trans. Geosci. Remote Sens.* **2023**, *61*, 1–14. [CrossRef]
7. Buehner, M.; Jacques, D. Non-Gaussian deterministic assimilation of radar-derived precipitation accumulations. *Mon. Weather. Rev.* **2020**, *148*, 783–808. [CrossRef]
8. Ravuri, S.; Lenc, K.; Willson, M.; Kangin, D.; Lam, R.; Mirowski, P.; Fitzsimons, M.; Athanassiadou, M.; Kashem, S.; Madge, S.; et al. Skilful precipitation nowcasting using deep generative models of radar. *Nature* **2021**, *597*, 672–677. [PubMed]
9. Mueller, C.; Saxen, T.; Roberts, R.; Wilson, J.; Betancourt, T.; Dettling, S.; Oien, N.; Yee, J. NCAR auto-nowcast system. *Weather. Forecast.* **2003**, *18*, 545–561. [CrossRef]
10. Austin, G.; Bellon, A. The use of digital weather radar records for short-term precipitation forecasting. *Q. J. R. Meteorol. Soc.* **1974**, *100*, 658–664.
11. Mecklenburg, S.; Joss, J.; Schmid, W. Improving the nowcasting of precipitation in an Alpine region with an enhanced radar echo tracking algorithm. *J. Hydrol.* **2000**, *239*, 46–68. [CrossRef]
12. Li, L.; Schmid, W.; Joss, J. Nowcasting of motion and growth of precipitation with radar over a complex orography. *J. Appl. Meteorol. Climatol.* **1995**, *34*, 1286–1300. [CrossRef]
13. del Moral, A.; Rigo, T.; Llasat, M.C. A radar-based centroid tracking algorithm for severe weather surveillance: Identifying split/merge processes in convective systems. *Atmos. Res.* **2018**, *213*, 110–120. [CrossRef]
14. Thu, N.V.; Tri, D.Q.; Hoa, B.T.K.; Nguyen-Thi, H.A.; Hung, N.V.; Tuyet, Q.T.T.; Van Nhat, N.; Pham, H.T. Application of optical flow technique to short-term rainfall forecast for some synoptic patterns in Vietnam. 2024; *Preprint*.
15. Smith, J.; Birch, C.; Marsham, J.; Peatman, S.; Bollasina, M.; Pankiewicz, G. Evaluating pySTEPS optical flow algorithms for convection nowcasting over the Maritime Continent using satellite data. *Nat. Hazards Earth Syst. Sci.* **2024**, *24*, 567–582. [CrossRef]
16. Chen, G.; Zhao, K.; Zhang, G.; Huang, H.; Liu, S.; Wen, L.; Yang, Z.; Yang, Z.; Xu, L.; Zhu, W. Improving polarimetric C-band radar rainfall estimation with two-dimensional video disdrometer observations in Eastern China. *J. Hydrometeorol.* **2017**, *18*, 1375–1391. [CrossRef]
17. Alfieri, L.; Claps, P.; Laio, F. Time-dependent ZR relationships for estimating rainfall fields from radar measurements. *Nat. Hazards Earth Syst. Sci.* **2010**, *10*, 149–158. [CrossRef]
18. Gultepe, I.; Sharman, R.; Williams, P.D.; Zhou, B.; Ellrod, G.; Minnis, P.; Trier, S.; Griffin, S.; Yum, S.S.; Gharabaghi, B.; et al. A review of high impact weather for aviation meteorology. *Pure Appl. Geophys.* **2019**, *176*, 1869–1921. [CrossRef]
19. Wilson, J.W.; Crook, N.A.; Mueller, C.K.; Sun, J.; Dixon, M. Nowcasting thunderstorms: A status report. *Bull. Am. Meteorol. Soc.* **1998**, *79*, 2079–2100. [CrossRef]
20. Habib, E.; Haile, A.T.; Tian, Y.; Joyce, R.J. Evaluation of the high-resolution CMORPH satellite rainfall product using dense rain gauge observations and radar-based estimates. *J. Hydrometeorol.* **2012**, *13*, 1784–1798. [CrossRef]
21. Sadeghi, M.; Nguyen, P.; Hsu, K.; Sorooshian, S. Improving near real-time precipitation estimation using a U-Net convolutional neural network and geographical information. *Environ. Model. Softw.* **2020**, *134*, 104856. [CrossRef]
22. An, S. Nowcast-to-Forecast: Token-Based Multiple Remote Sensing Data Fusion for Precipitation Forecast. In Proceedings of the 32nd ACM International Conference on Information and Knowledge Management, Birmingham, UK, 21–25 October 2023; pp. 4495–4501.
23. Sun, Q.; Miao, C.; Duan, Q.; Ashouri, H.; Sorooshian, S.; Hsu, K.L. A review of global precipitation data sets: Data sources, estimation, and intercomparisons. *Rev. Geophys.* **2018**, *56*, 79–107. [CrossRef]
24. Zeng, X. The relationship among precipitation, cloud-top temperature, and precipitable water over the tropics. *J. Clim.* **1999**, *12*, 2503–2514. [CrossRef]
25. Anagnostou, E.N.; Negri, A.J.; Adler, R.F. A satellite infrared technique for diurnal rainfall variability studies. *J. Geophys. Res. Atmos.* **1999**, *104*, 31477–31488.
26. Delgado, G.; Machado, L.A.; Angelis, C.F.; Bottino, M.J.; Redano, A.; Lorente, J.; Gimeno, L.; Nieto, R. Basis for a rainfall estimation technique using IR–VIS cloud classification and parameters over the life cycle of mesoscale convective systems. *J. Appl. Meteorol. Climatol.* **2008**, *47*, 1500–1517. [CrossRef]
27. Ma, Z.; Zhang, H.; Liu, J. MS-RNN: A Flexible Multi-Scale Framework for Spatiotemporal Predictive Learning. *arXiv* **2024**, arXiv:2206.03010.
28. LeCun, Y.; Bengio, Y.; Hinton, G. Deep learning. *Nature* **2015**, *521*, 436–444. [CrossRef]
29. Behrens, G.; Beucler, T.; Iglesias-Suarez, F.; Yu, S.; Gentine, P.; Pritchard, M.; Schwabe, M.; Eyring, V. Improving Atmospheric Processes in Earth System Models with Deep Learning Ensembles and Stochastic Parameterizations. *arXiv* **2024**, arXiv:2402.03079.
30. Wang, L.Y.; Tan, Z.M. Deep learning parameterization of the tropical cyclone boundary layer. *J. Adv. Model. Earth Syst.* **2023**, *15*, e2022MS003034. [CrossRef]
31. Ham, Y.G.; Kim, J.H.; Luo, J.J. Deep learning for multi-year ENSO forecasts. *Nature* **2019**, *573*, 568–572. [CrossRef] [PubMed]

32. Wang, T.; Huang, P. Superiority of a convolutional neural network Model over Dynamical models in Predicting Central Pacific ENSO. *Adv. Atmos. Sci.* **2024**, *41*, 141–154. [CrossRef]
33. Ibebuchi, C.C.; Richman, M.B. Deep learning with autoencoders and LSTM for ENSO forecasting. *Clim. Dyn.* **2024**, 1–15. [CrossRef]
34. Tan, J.; Huang, Q.; Chen, S. Deep learning model based on multi-scale feature fusion for precipitation nowcasting. *Geosci. Model Dev.* **2024**, *17*, 53–69. [CrossRef]
35. Zhang, Y.; Long, M.; Chen, K.; Xing, L.; Jin, R.; Jordan, M.I.; Wang, J. Skilful nowcasting of extreme precipitation with NowcastNet. *Nature* **2023**, *619*, 526–532. [CrossRef] [PubMed]
36. Ma, Z.; Zhang, H.; Liu, J. Db-rnn: A rnn for precipitation nowcasting deblurring. *IEEE J. Sel. Top. Appl. Earth Obs. Remote Sens.* **2024**, *17*, 5026–5041. [CrossRef]
37. Küçük, Ç.; Giannakos, A.; Schneider, S.; Jann, A. Nowcasting with Transformer-based Models using Multi-Source Data. Technical report, Copernicus Meetings. 2024. Available online: https://meetingorganizer.copernicus.org/EGU24/EGU24-7536.html (accessed on 3 August 2024). [CrossRef]
38. Jin, Q.; Zhang, X.; Xiao, X.; Wang, Y.; Xiang, S.; Pan, C. Preformer: Simple and Efficient Design for Precipitation Nowcasting with Transformers. *IEEE Geosci. Remote Sens. Lett.* **2023**, *21*, 1000205. [CrossRef]
39. Shi, X.; Chen, Z.; Wang, H.; Yeung, D.Y.; kin Wong, W.; chun Woo, W. Convolutional LSTM Network: A Machine Learning Approach for Precipitation Nowcasting. *arXiv* **2015**, arXiv:1506.04214.
40. Agrawal, S.; Barrington, L.; Bromberg, C.; Burge, J.; Gazen, C.; Hickey, J. Machine Learning for Precipitation Nowcasting from Radar Images. *arXiv* **2019**, arXiv:1912.12132.
41. Ma, Z.; Zhang, H.; Liu, J. Focal frame loss: A simple but effective loss for precipitation nowcasting. *IEEE J. Sel. Top. Appl. Earth Obs. Remote Sens.* **2022**, *15*, 6781–6788. [CrossRef]
42. Ehsani, M.R.; Zarei, A.; Gupta, H.V.; Barnard, K.; Lyons, E.; Behrangi, A. NowCasting-Nets: Representation learning to mitigate latency gap of satellite precipitation products using convolutional and recurrent neural networks. *IEEE Trans. Geosci. Remote Sens.* **2022**, *60*, 1–21. [CrossRef]
43. An, S.; Oh, T.J.; Sohn, E.; Kim, D. Deep learning for precipitation nowcasting: A survey from the perspective of time series forecasting. *arXiv* **2024**, arXiv:2402.13737.
44. Reulen, E.; Mehrkanoon, S. GA-SmaAt-GNet: Generative Adversarial Small Attention GNet for Extreme Precipitation Nowcasting. *arXiv* **2024**, arXiv:2401.09881.
45. Gao, Z.; Shi, X.; Han, B.; Wang, H.; Jin, X.; Maddix, D.; Zhu, Y.; Li, M.; Wang, Y.B. Prediff: Precipitation nowcasting with latent diffusion models. *Adv. Neural Inf. Process. Syst.* **2023**, *36*, 78621–78656.
46. Ling, X.; Li, C.; Qin, F.; Yang, P.; Huang, Y. SRNDiff: Short-term Rainfall Nowcasting with Condition Diffusion Model. *arXiv* **2024**, arXiv:2402.13737.
47. Dehghani, M.; Djolonga, J.; Mustafa, B.; Padlewski, P.; Heek, J.; Gilmer, J.; Steiner, A.P.; Caron, M.; Geirhos, R.; Alabdulmohsin, I.; et al. Scaling Vision Transformers to 22 Billion Parameters. In Proceedings of the International Conference on Machine Learning, Honolulu, HI, USA, 23–29 July 2023; pp. 7480–7512.
48. Kurth, T.; Subramanian, S.; Harrington, P.; Pathak, J.; Mardani, M.; Hall, D.; Miele, A.; Kashinath, K.; Anandkumar, A. Fourcastnet: Accelerating Global High-Resolution Weather Forecasting using Adaptive Fourier Neural Operators. In Proceedings of the Platform for Advanced Scientific Computing Conference, Davos, Switzerland, 26–28 June 2023; pp. 1–11.
49. Bai, C.; Sun, F.; Zhang, J.; Song, Y.; Chen, S. Rainformer: Features Extraction Balanced Network for Radar-Based Precipitation Nowcasting. *IEEE Geosci. Remote Sens. Lett.* **2022**, *19*, 1–5. [CrossRef]
50. Gao, Z.; Shi, X.; Wang, H.; Zhu, Y.; Wang, Y.; Li, M.; Yeung, D.Y. Earthformer: Exploring Space-Time Transformers for Earth System Forecasting. *arXiv* **2023**, arXiv:2207.05833.
51. Harrer, S. Attention is not all you need: The complicated case of ethically using large language models in healthcare and medicine. *EBioMedicine* **2023**, *90*, 104512. [CrossRef] [PubMed]
52. Woo, W.; Wong, W. Application of Optical Flow Techniques to Rainfall Nowcasting. In Proceedings of the the 27th Conference on Severe Local Storms, Madison, WI, USA, 3–7 November 2014.
53. Lee, Y.; Kummerow, C.D.; Ebert-Uphoff, I. Applying machine learning methods to detect convection using Geostationary Operational Environmental Satellite-16 (GOES-16) advanced baseline imager (ABI) data. *Atmos. Meas. Tech.* **2021**, *14*, 2699–2716. [CrossRef]
54. Shi, X.; Gao, Z.; Lausen, L.; Wang, H.; Yeung, D.Y.; kin Wong, W.; chun Woo, W. Deep Learning for Precipitation Nowcasting: A Benchmark and A New Model. *arXiv* **2017**, arXiv:1706.03458.
55. Sønderby, C.K.; Espeholt, L.; Heek, J.; Dehghani, M.; Oliver, A.; Salimans, T.; Agrawal, S.; Hickey, J.; Kalchbrenner, N. MetNet: A Neural Weather Model for Precipitation Forecasting. *arXiv* **2020**, arXiv:2003.12140.
56. Wang, Y.; Gao, Z.; Long, M.; Wang, J.; Philip, S.Y. Predrnn++: Towards a Resolution of the Deep-in-Time Dilemma in Spatiotemporal Predictive Learning. In Proceedings of the International Conference on Machine Learning, Stockholm Sweden, 10–15 July 2018; pp. 5123–5132.
57. Wang, Y.; Long, M.; Wang, J.; Gao, Z.; Yu, P.S. PredRNN: Recurrent neural networks for predictive learning using spatiotemporal LSTMs. *Adv. Neural Inf. Process. Syst.* **2017**, *30*, 879–888.

58. Wu, H.; Yao, Z.; Wang, J.; Long, M. MotionRNN: A Flexible Model for Video Prediction with Spacetime-Varying Motions. In Proceedings of the IEEE/CVF Conference on Computer Vision and Pattern Recognition, Nashville, TN, USA, 20–25 June 2021; pp. 15435–15444.
59. Bihlo, A. A generative adversarial network approach to (ensemble) weather prediction. *Neural Netw.* **2021**, *139*, 1–16. [CrossRef]
60. Tang, C.; Salakhutdinov, R.R. Multiple futures prediction. *arXiv* **2019**, arXiv:1911.00997.
61. Lagerquist, R.; Stewart, J.Q.; Ebert-Uphoff, I.; Kumler, C. Using deep learning to nowcast the spatial coverage of convection from Himawari-8 satellite data. *Mon. Weather. Rev.* **2021**, *149*, 3897–3921.
62. Weyn, J.A.; Durran, D.R.; Caruana, R. Improving data-driven global weather prediction using deep convolutional neural networks on a cubed sphere. *J. Adv. Model. Earth Syst.* **2020**, *12*, e2020MS002109. [CrossRef]
63. Zhou, K.; Zheng, Y.; Dong, W.; Wang, T. A deep learning network for cloud-to-ground lightning nowcasting with multisource data. *J. Atmos. Ocean. Technol.* **2020**, *37*, 927–942. [CrossRef]
64. Jones, R.; Thornton, J.; Durran, D.; Jaeglé, L.; Wright, C.; Holzworth, R. A Deep Learning Approach to Lightning Nowcasting and Forecasting. In Proceedings of the EGU General Assembly 2024, Vienna, Austria, 14–19 April 2024.
65. Li, J.; Li, L.; Zhang, T.; Xing, H.; Shi, Y.; Li, Z.; Wang, C.; Liu, J. Flood forecasting based on radar precipitation nowcasting using U-net and its improved models. *J. Hydrol.* **2024**, *632*, 130871. [CrossRef]
66. Rahimi, R.; Ravirathinam, P.; Ebtehaj, A.; Behrangi, A.; Tan, J.; Kumar, V. Global Precipitation Nowcasting of Integrated Multi-satellitE Retrievals for GPM: A U-Net Convolutional LSTM Architecture. *J. Hydrometeorol.* **2024**, *25*, 947–963. [CrossRef]
67. Niu, D.; Li, Y.; Wang, H.; Zang, Z.; Jiang, M.; Chen, X.; Huang, Q. FsrGAN: A Satellite and Radar-Based Fusion Prediction Network for Precipitation Nowcasting. *IEEE J. Sel. Top. Appl. Earth Obs. Remote Sens.* **2024**, *17*, 7002–7013. [CrossRef]
68. Huffman, G.J.; Bolvin, D.T.; Braithwaite, D.; Hsu, K.L.; Joyce, R.J.; Kidd, C.; Nelkin, E.J.; Sorooshian, S.; Stocker, E.F.; Tan, J.; et al. Integrated multi-satellite retrievals for the global precipitation measurement (GPM) mission (IMERG). *Satell. Precip. Meas.* **2020**, *1*, 343–353.
69. Global Climate and Weather Modeling Branch. *The GFS Atmospheric Model*; Technical Report 442; NCEP Office Note; NCEP Office: Camp Springs, MD, USA, 2003.
70. Oktay, O.; Schlemper, J.; Folgoc, L.L.; Lee, M.; Heinrich, M.; Misawa, K.; Mori, K.; McDonagh, S.; Hammerla, N.Y.; Kainz, B.; et al. Attention U-Net: Learning Where to Look for the Pancreas. *arXiv* **2018**, arXiv:1804.03999.
71. Alom, M.Z.; Hasan, M.; Yakopcic, C.; Taha, T.M.; Asari, V.K. Recurrent Residual Convolutional Neural Network based on U-Net (R2U-Net) for Medical Image Segmentation. *arXiv* **2018**, arXiv:1802.06955.
72. Azad, R.; Aghdam, E.K.; Rauland, A.; Jia, Y.; Avval, A.H.; Bozorgpour, A.; Karimijafarbigloo, S.; Cohen, J.P.; Adeli, E.; Merhof, D. Medical Image Segmentation Review: The success of U-Net. *arXiv* **2022**, arXiv:2211.14830.
73. Jumianti, N.; Marzuki, M.; Yusnaini, H.; Ramadhan, R.; Harjupa, W.; Saufina, E.; Nauval, F.; Risyanto, R.; Sakti, A.D.; Abdillah, M.R.; et al. Prediction of extreme rain in Kototabang using Himawari-8 satellite based on differences in cloud brightness temperature. *Remote Sens. Appl. Soc. Environ.* **2024**, *33*, 101102. [CrossRef]
74. Bessho, K.; Date, K.; Hayashi, M.; Ikeda, A.; Imai, T.; Inoue, H.; Kumagai, Y.; Miyakawa, T.; Murata, H.; Ohno, T.; et al. An introduction to Himawari-8/9—Japan's new-generation geostationary meteorological satellites. *J. Meteorol. Soc. Jpn. Ser. II* **2016**, *94*, 151–183. [CrossRef]
75. Schaefer, J.T. The critical success index as an indicator of warning skill. *Weather. Forecast.* **1990**, *5*, 570–575. [CrossRef]
76. Skees, P.; Shenton, L. Comments on the statistical distribution of rainfall per period under various transformations. *USDA Misc. Publ.* **1974**, *1275*, 172–196.
77. McCune, B.; Grace, J.B.; Urban, D.L. *Analysis of Ecological Communities*; MjM Software Design: Gleneden Beach, OR, USA, 2002; Volume 28.
78. Jin, Q.; Meng, Z.; Sun, C.; Wei, L.; Su, R. RA-UNet: A hybrid deep attention-aware network to extract liver and tumor in CT scans. *arXiv* **2018**, arXiv:1811.01328.
79. Ronneberger, O.; Fischer, P.; Brox, T. U-Net: Convolutional Networks for Biomedical Image Segmentation. *arXiv* **2015**, arXiv:1505.04597.
80. Lee, T.; Kong, Y.; Lee, J.H.; Yoon, H.C. Spring precipitation forecasting with exhaustive searching and LASSO using climate teleconnection for drought management. *Clim. Dyn.* **2024**, *62*, 1625–1648. [CrossRef]
81. Lee, Y.; Kummerow, C.D.; Zupanski, M. A simplified method for the detection of convection using high-resolution imagery from GOES-16. *Atmos. Meas. Tech.* **2021**, *14*, 3755–3771. [CrossRef]
82. Sun, D.; Huang, W.; Yang, Z.; Luo, Y.; Luo, J.; Wright, J.S.; Fu, H.; Wang, B. Deep learning improves GFS wintertime precipitation forecast over southeastern China. *Geophys. Res. Lett.* **2023**, *50*, e2023GL104406. [CrossRef]